Received: 4 December 2023 | Revised: 7 July 2024 | Accepted: 10 July 2024

DOI: 10.1002/qj.4818

Quarterly Journal of the Royal Meteorological Society RMetS

RESEARCH ARTICLE

Evaluation of near-surface and boundary-layer meteorological conditions that support cold-fog formation using Cold Fog Amongst Complex Terrain field campaign observations

Rebecca Lynn Beal[1] | **Zhaoxia Pu**[1] | **Eric Pardyjak**[2] | **Sebastian Hoch**[1] | **Ismail Gultepe**[3]

[1]Department of Atmospheric Sciences, University of Utah, Salt Lake City, Utah, USA

[2]Department of Mechanical Engineering, University of Utah, Salt Lake City, Utah, USA

[3]Faculty of Engineering and Applied Science, and ACE, Ontario Technical University, Oshawa, Ontario Canada

Correspondence
Zhaoxia Pu, Department of Atmospheric Sciences, University of Utah, Salt Lake City, UT, USA.
Email: zhaoxia.pu@utah.edu

Funding information
National Science Foundation, Grant/Award Number: #2049100

Abstract

Cold fog refers to a type of fog that forms when the temperature is below 0°C. It can be composed of liquid, ice, and mixed-phase fog particles. Cold fog happens frequently over mountainous terrain in the cold season, but it is difficult to predict. Using observations from the Cold Fog Amongst Complex Terrain (CFACT) field campaign conducted in Heber Valley, Utah, in the western United States during January and February of 2022, this study investigates the meteorological conditions in the surface and boundary layers that support the formation of wintertime ephemeral cold fog in a local area of small-scale mountain valleys. It is found that fog formation is susceptible to subtleties in forcing conditions and is supported by several factors: (1) established high pressure over the Great Basin with associated local clear skies, calm winds, and a stable boundary layer; (2) near-surface inversion with saturation near the surface and strong moisture gradient in the boundary layer; (3) warm (above-freezing) daytime air temperature with a large diurnal range, accompanied with warm soil temperatures during the daytime; (4) a period of increased turbulence kinetic energy (above 0.5 $m^2 \cdot s^{-2}$), followed by calm conditions throughout the fog's duration; and (5) supersaturation with respect to ice. Then, the field observations and identified supporting factors for fog formation were utilized to evaluate high-resolution (~400 m horizontal grid spacing) Weather Research and Forecasting (WRF) model simulations. Results show that the WRF model accurately simulates the mesoscale conditions facilitating cold-fog formation but misses some critical surface and atmospheric boundary conditions. The overall results from this paper indicate that these identified factors that support fog formation are vital to accurately forecasting cold-fog events. At the same time, they are also critical fields for the NWP model validation.

KEYWORDS

boundary layer, CFACT, cold fog, Heber Valley, turbulence, WRF

1 | INTRODUCTION

Fog, which consists of droplets or ice crystals, is a localized weather event that occurs when near-surface visibility is reduced below 1 km (American Meteorological Society, 2012). Fog poses significant and costly dangers to various aspects of daily life, particularly transportation (Gultepe et al., 2007, 2017). According to statistics from the U.S. Federal Highway Administration (2020), fog is responsible for over 25,000 car crashes annually, resulting in nearly 10,000 injuries and 500 deaths (2020). This is comparable to the total number of deaths from all other weather-related hazards combined (National Weather Service, 2022). Poor visibility and icing risks heavily impact aviation during hazardous cold-fog events (Gultepe et al., 2014). Fog and low visibility are the second most common factors in aviation weather-related accidents (Federal Aviation Administration, 2010) and the most fatal (Fultz & Ashley, 2016). In addition, while over 300 fatal car crashes occurred in foggy conditions, 72% of these incidents happened without National Weather Service (NWS) fog advisories being issued. *This underscores the urgent need for improving fog forecasts* (Ashley et al., 2015). These problems become even more severe during mountainous cold fog, forming under below-freezing temperatures, due to its complexity in physical processes involved, mixed-phase fog particles, and interaction with complex terrain (Ducongé et al., 2020; Golding, 1993; Gultepe et al., 2009; Prtenjak et al., 2018; Pu et al., 2023; Wei et al., 2013). Therefore, it is essential to understand the complex processes related to fog, especially fog over complex terrain, through comprehensive observational or modeling studies.

In practice, understanding fog formation and evolution is crucial to improving fog forecasting and mitigating fog-related risks. In general, fog forms under the intersection of many physical, dynamic, and microphysical processes. The cold fog in mountainous terrain can further complicate these conditions due to complicated interactions between different processes as well as complex topography (Gultepe et al., 2007, 2009, 2014, 2016, 2017; 2021, Price et al., 2018; Pu et al., 2016, 2023). Hodges and Pu (2015) examined the climatology surrounding cold-fog events over the Heber Valley, Utah, the United States. They outlined the ideal conditions for Heber's wintertime fog with regard to the synoptic weather patterns: a high-pressure center over the Great Basin region with associated clear skies and calm winds that lead to a temperature inversion and a stable boundary layer. Other studies found that since fog forms close to the surface, errors in the near-surface and boundary-layer conditions from numerical model simulations can lead to inaccurate fog forecasts (Pu et al., 2016; Smith et al., 2020; Steeneveld et al., 2015; Zhang & Pu, 2019). Comprehensive observations are needed to study the processes that lead to fog formation and to validate model simulations. However, until recently, few observations in the near-surface and boundary-layer atmosphere have supported investigations into cold-fog formation.

Numerous field campaigns have been conducted around the world across various types of terrain and climate zones to study local conditions for fog formation, evolution, and dissipation (Adedokun & Holmgren, 1993; Cuxart & Jiménez, 2012; Fernando et al., 2021; Fitzjarrald & Lala, 1989; Fuzzi et al., 1992; Ghude et al., 2017; Gultepe et al., 2009; Gultepe et al., 2016; Holets & Swanson, 1981; Noonkester, 1979; Price et al., 2018; Underwood et al., 2004). Among these field campaigns, a portion of the MATERHORN project (Fernando & Pardyjak, 2015) took place in Heber Valley (known as MATERHORN-fog, Gultepe et al., 2016) utilizing microphysical instruments and radiosoundings to study cold fog in complex terrain. The field observations and analyses highlighted the need for high spatial and temporal resolution of local surface and boundary-layer conditions in Heber Valley (Hang et al., 2016). They also underscored the urgency of further validating numerical weather prediction models, such as the mesoscale Weather Research and Forecasting (WRF) model, as the WRF model missed nearly all fog events in real-time forecasts.

Motivated by the findings from MATERHORN-fog and the need to better understand cold fog over mountainous valleys, the Cold Fog Amongst Complex Terrain (CFACT) field campaign was carried out in Heber Valley, Utah, from 7 January to 23 February, 2022 (Pu et al., 2023). The CFACT field campaign consisted of an array of meteorological towers and remote-sensing platforms measuring radiative fluxes, surface energy balance, and near-surface turbulence fluxes, and radiosondes. In this study, we examine the near-surface and atmospheric boundary-layer meteorological conditions that support fog formation with CFACT observations for the first time. The performance of WRF model fog prediction is also evaluated. Specifically, as documented in Pu et al. (2023), because nearly all fog events during CFACT occurred near the Deer Creek Supersite (DC SS), located on the floor of Heber Valley near moisture sources (e.g., Deer Creek Reservoir. see Figure 1a), and most CFACT instrumentation and radiosondes were deployed at that site, the analysis of this study emphasizes the DC SS. Four out of nine total CFACT Intensive Observing Periods (IOPs) are examined, including two IOPs with fog (6 and 8) and two clear events (IOPs 3 and 7 with no fog). Specifically, we characterize the near-surface and boundary-layer meteorological conditions during fog and clear events, identifying the conditions supporting fog formation. Then, the model

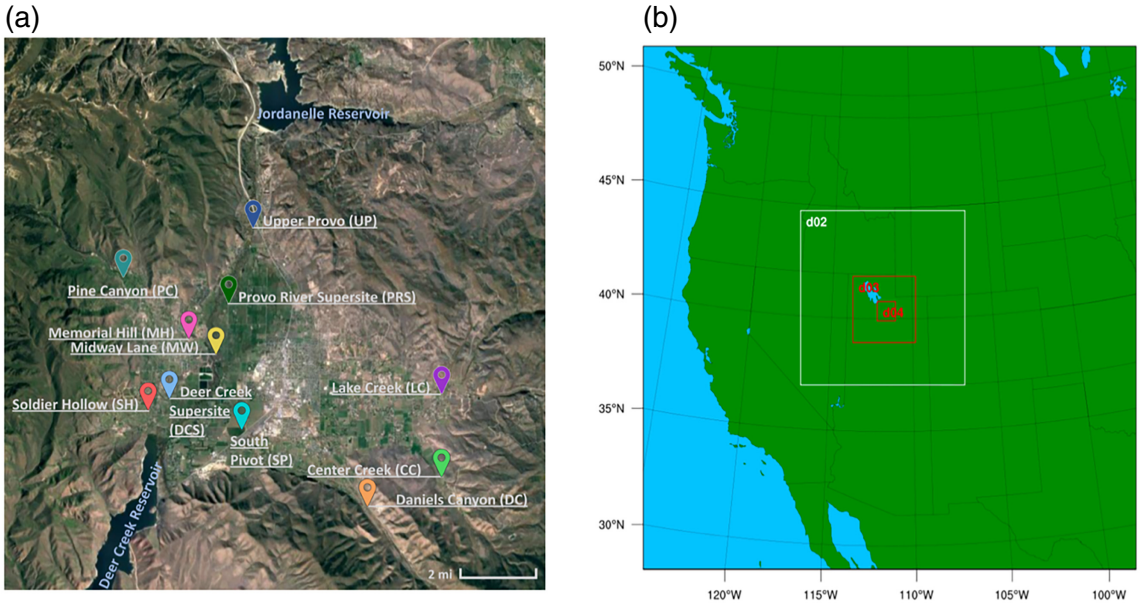

FIGURE 1 (a) Heber Valley and its vicinity with locations mentioned in the paper, including the Provo River and its tributaries that flow south into the Deer Creek Reservoir. (b) The location of Weather Research and Forecasting (WRF) domains. Note that panel (a) is located as part of domain 4 (d04). The area covers the center of d04 for about one-third of the total area of d04.

deficiencies in forecasting fog are assessed by comparing the CFACT observations with the WRF simulations.

Section 2 | outlines the CFACT observations and analysis methodology. Section 3 | describes the synoptic weather background of selected cases. Section 4 | analyzes each case's near-surface and planetary boundary layer (PBL) conditions. Section 5 | presents an evaluation of the high-resolution WRF simulations. Section 6 | summarizes the findings from this study and discusses additional areas for further work.

2 | DATA AND CASES

During the CFACT field campaign (Pu et al., 2023), comprehensive sets of instrumentation were deployed at the DC SS (40.490101° N, 111.464737° W) to measure various meteorological, physical, microphysical, and air chemistry variables (see details in Pu et al., 2023). The meteorological variables at the DC SS were measured by a surface station and 3- and 32-m towers. Net longwave radiation measurements were also made at 0.5 and 32 m above ground level. During IOPs, radiosondes were released every tree hours for 24 h, beginning at 2100 UTC (1400 local time, or U.S. Mountain Standard Time, MST).

A real-time forecast with the mesoscale community WRF model (version 4.3; Skamarock et al., 2021) was executed during the field campaign in multiscale nested domains (12, 4, 1.33 km, and 444.4 m grid resolution; Figure 1b) at grid dimensions of 211×211, 211×211, 241×241, and 211×211, respectively. The innermost domain (~444.4 m) was used to produce a local forecast in Heber Valley and its vicinity. Vertically, the model was set up with 56 levels (the top of the model was set to 50 hPa), with the lowest level at 15 m and nine levels in the lower boundary layer below 200 m. The physical parameterization schemes (detailed in Skamarock et al., 2021) included the Kain–Fritsch cumulus scheme (for 12-km grid spacing only), the Thompson microphysics scheme, the Rapid Radiative Transfer Model (RRTM) for longwave radiation, and the Dudhia scheme for shortwave radiation. The Noah land surface model was used. The Yonsei University (YSU) PBL scheme was adopted for 12, 4, and 1.33 km grid spacing for its ability to generate relatively accurate turbulence mixing. For domain 4, instead of the PBL scheme, a 3D Turbulence Kinetic Energy subgrid mixing scheme (SMS-3DTKE) was used to allow for self-adaptation to the grid size between the large-eddy simulation and mesoscale limits (Juliano et al., 2022). Initial and boundary conditions were derived from the real-time NCEP North American Mesoscale (NAM) model analysis and forecasts (available at 12 km horizontal grid resolution), and 72-hr forecasts were performed daily at 0000 UTC and 1200 UTC during the CFACT field campaign.

Of the nine IOPs during the CFACT, four were chosen for analysis in this study: IOPs 3 (19–20 January), 6 (12–13 February), 7 (17–18 February), and 8 (18–19 February). According to observations (Pu et al., 2023), localized,

shallow, ephemeral fog occurred during IOPs 6 and 8 and was observed at the DC SS, while IOPs 3 and 7 remained clear. IOPs 3, 7, and 8 were predicted during the field campaign as fog cases, while IOP 6 was forecasted as a clear, quiescent case. Therefore, the four selected cases represent fog and null fog cases in both observations and model forecasts. While fog cases represent favorable conditions for fog formation, the null fog cases are also informative. For instance, fog occurred in several nearby valleys preceding and during 19–20 January 2022, indicating that large-scale weather conditions during IOP 3 supported fog while local conditions did not. IOP 7 (a null fog case) occurred only a day before IOP 8 (a fog case) under a similar large-scale weather pattern.

3 | SYNOPTIC BACKGROUND AND MESOSCALE ENVIRONMENT

During the 2021–2022 winter season, Utah, as well as most of the western U.S., was under a severe drought (National Drought Mitigation Center, 2022) and faced unseasonably dry conditions. The drought suppressed fog opportunities. In January 2022, Heber Valley overall received only 50% of normal precipitation (snow), and nearly all of it fell before the beginning of the field campaign on 7 January. Then, in February, precipitation reached only 34% of the normal level (Clayton et al., 2022a, 2022b). During the CFACT field campaign, Utah frequently experienced stationary high-pressure ridges over the Great Basin that created a strong, persistent ridge (trough) pattern across the western (eastern) U.S. These ridges forced the winter jet stream north, channeling storms away and blocking them from affecting Utah. For most of the campaign, the weather was dry, with occasional disruptions from weak shortwaves and cold fronts. There were a few periods of light snow, but most events produced trace snowfall without accumulation.

During IOP 3, the valley floor had patchy snow from the previous winter storms that occurred on 7 January 2022. The surrounding water sources, such as the Deer Creek Reservoir (close to the DC SS, see Figure 1a), were ice-free. A synoptic high pressure settled over the western U.S. from 14 to 19 January, causing persistent valley inversions to form. Haze built up during the multiday inversion event, and fog repeatedly formed overnight across much of northern Utah (except for Heber Valley) from 14 to 21 January, including nearby valleys (e.g., the Wasatch Front, Bear River Valley). From 18 to 19 January, strong northwesterly flow brought upper and mid-level clouds to northern Utah, but the Wasatch Mountains blocked low-level moisture (Figure 2a). The high pressure re-established on the afternoon of 19 January, with overcast conditions persisting for much of IOP 3.

IOP 6 occurred during the snow drought, with the last snowfall on 2 February, under a strong high-pressure system (Figure 2b). The center of this high-pressure system was located over southwestern Colorado and surrounding areas, including northern Utah. Local conditions were dry and clear following several days of warm air advection. Ice covered the Jordanelle Reservoir, while small sections of open water remained at the Deer Creek Reservoir. From 4 to 11 February, persistent cold air pools within the topographic basins across northern Utah led to widespread haze. Above-freezing daytime temperatures led to the melting of the little existing snow. On the afternoon of 11 February, a dry shortwave trough led to upper-level cooling, eroding the capping inversion and mixing out the haze in the valleys. The high pressure re-asserted itself, with warm air advection leading to rapid re-assertion of the capping inversion over Heber Valley. Fog formed early on 13 February for a few hours between 0845 and 1400 UTC.

Prior to IOP 7, a light snow event (no snow accumulation) on 16 February brought surface moisture to northern Utah (Figure 2c). Localized pockets of high relative humidity were mostly driven by terrain, with local valleys highlighted, including Heber Valley. Strong winds and cloud cover persisted throughout 17 February and began to dissipate overnight. Winds remained calm for the duration of IOP 7, though two periods of passing mid-level clouds interrupted the nocturnal cooling cycle, and no fog formed during IOP 7. IOP 8 happened the following night after the high-pressure system fully re-asserted itself over northern Utah following the storm's passage on 16 February (Figure 2d). Large-scale drying and moderate warming trends were evident between IOP 7 and IOP 8. Due to warm air advection, a subsidence inversion was fully re-established. Clear skies, warmer daytime temperatures, and calm conditions allowed fog to form late on 18 February until the early morning of 19 February, between 0530 and 1500 UTC.

4 | NEAR-SURFACE AND BOUNDARY-LAYER CONDITIONS

4.1 | Boundary-layer evolution

Figure 3 illustrates the evolution of atmospheric temperature and humidity profiles during the IOPs, highlighting the evolution of the boundary layer in each case. During IOP 3, a deep, saturated near-isothermal layer formed in the morning on 20 February (e.g., between 0900 and 1400 UTC) due to a subsidence inversion dropping and a surface inversion deepening, eventually joining together

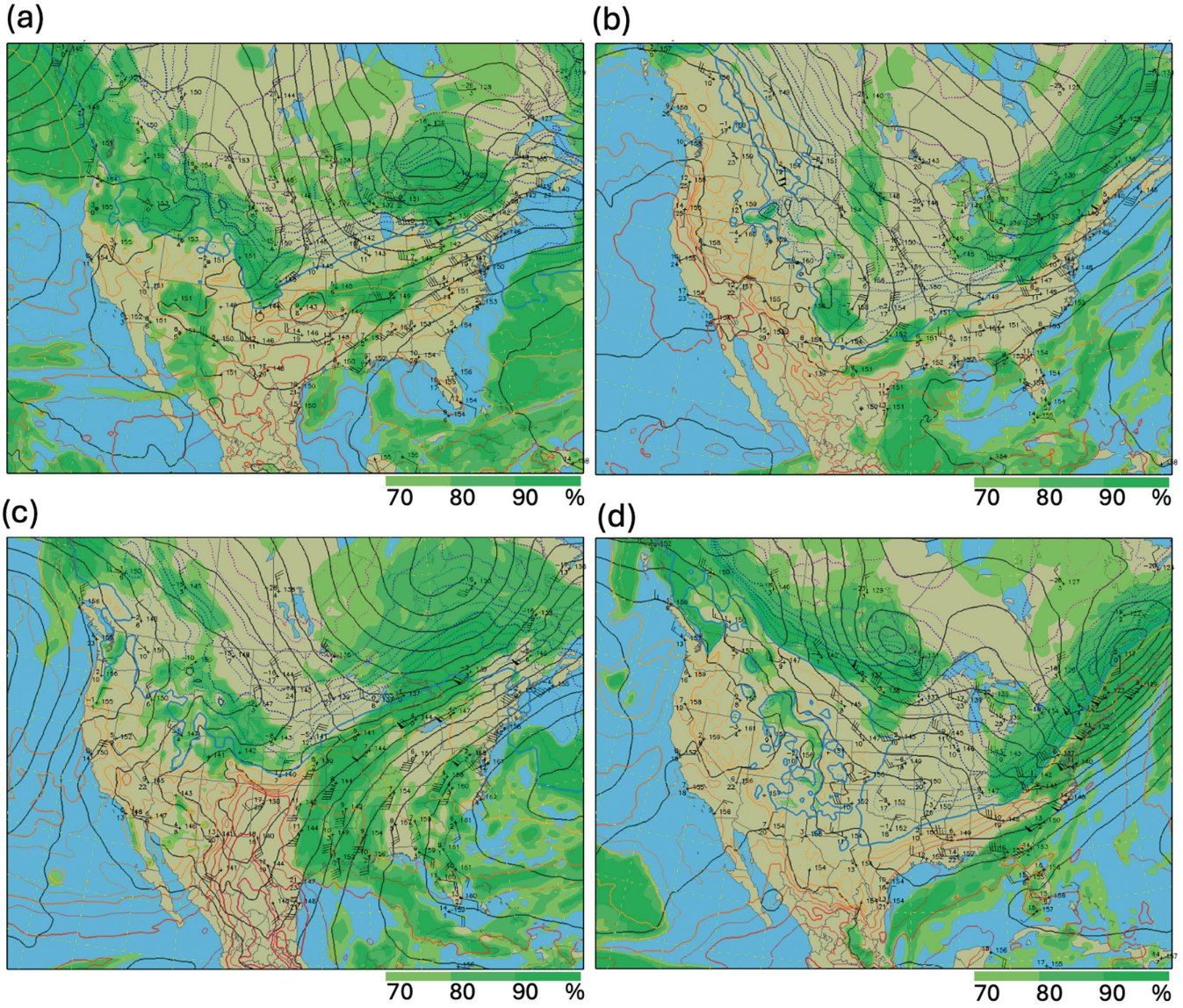

FIGURE 2 Synoptic weather maps at 850 hPa, generated from NOAA rapid refresh (RAP) analysis, showing contoured heights (black), temperature (colored lines), and relative humidity (shaded green) for IOP 3 valid at 12 UTC 19 Jan 2022 (a), IOP 6 valid at 12 UTC 12 Feb 2022 (b), IOP 7 valid at 00 UTC 17 Feb 2022 (c), and IOP 8 valid at 12 UTC 18 Feb 2022 (d).

(Figure 3a,b). At 2100 UTC on 19 January, there was a shallow capping inversion at approx. 750 hPa. Over time, the capping inversion dropped closer to the surface, and the inversion's base eroded. Around 0500 UTC, a surface inversion formed and developed, eventually meeting the capping inversion. At around 1100 UTC, the mixed layer extended from the surface to 500 hPa. As the lower-level atmosphere mixed, isothermal and more saturated conditions developed. The basin cold pool (up to 700 hPa) became more moist until the entire inversion layer was nearly saturated by 1400 UTC, 20 February. Then, the inversion broke down after sunrise, and the near-surface air became dry again.

IOP 6 was characterized by limited mixing in the boundary layer (Figure 3c,d). The surface-based inversion strengthened overnight as the surface temperature dropped, reaching a much weaker capping inversion that quickly lowered from 650 hPa at 2100 UTC, 12 February to around 750 hPa by 2300 UTC, while the surface exhibited a drying trend. Then, at 0200 UTC on 13 February, a surface inversion formed as the relative humidity increased from approx. 20% to approx. 60%, partly due to the surface radiative cooling. As the surface inversion deepened to approx. 750 hPa and mixed with the weak capping inversion, relative humidity continued to increase, reaching saturation at the surface by 1100 UTC, 13 February. Fog

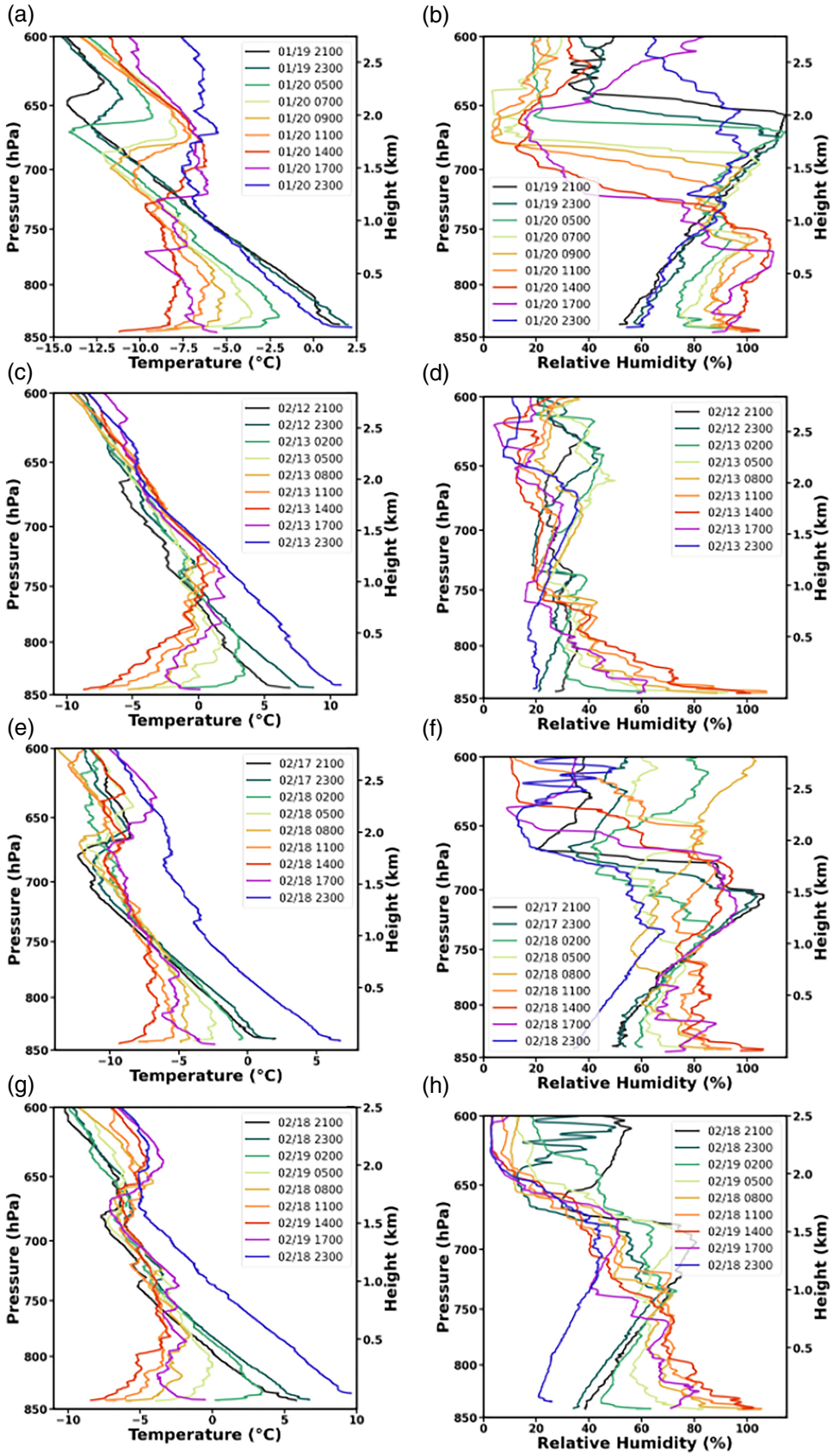

FIGURE 3 Overlaid radiosonde soundings released at the Deer Creek Supersite (DC SS) during Intensive Observing Periods (IOPs). (a) and (b) for IOP 3 (a null fog case); (c) and (d) for IOP 6 (a fog case); (e) and (f) for IOP 7 (a null fog case); and (g) and (h) for IOP 8 (a fog case). (a, c, e, g) are for temperature and (b, d, f, h) for relative humidity with respect to ice, respectively. Each panel's date and time format is denoted as "month/date UTC."

formed from roughly 0900 to 1400 UTC, almost as soon as the near-surface reached saturation with respect to ice.

The boundary-layer evolutions during IOP 7 were not steady (Figure 3e,f). Early surface inversion began at 0200 UTC. Then, it strengthened over time while still remaining very shallow (~830 hPa). The base of the initial capping inversion (~675 hPa) weakened from 2100 UTC, 17 February to 0200 UTC, 18 February. Eventually, a near-isothermal layer formed from 700 to 600 hPa. Another small subsidence inversion previously at approx. 625 hPa quickly strengthened and replaced the first capping inversion by 0500 UTC and extended from approx. 700 to 650 hPa. The subsequent evolution of this inversion was marked by rapid weakening by 0800 UTC and another weak subsidence inversion forming at approx. 575 hPa. By 1100 UTC on 18 February, the well-mixed, near-isothermal layer extended from 650 to 825 hPa, and the remaining capping inversion lowered to approx. 600 hPa. These ongoing evolutions in the boundary layer led to several distinct layers with different relative humidity characteristics. Saturation at the surface was reached as the near-surface temperature decreased due to the radiative cooling. Above the surface, the first and second capping inversions weakened, significant mixing took place (1100 UTC, 18 February), and the entire layer, up to 650 hPa, became more humid, but it did not reach saturation.

During IOP 8 (Figure 3g,h), a deep, stable boundary layer formed, and limited mixing led to stratified saturation conditions with saturation near the surface and dry conditions above. A weak capping inversion at around 650 hPa persisted for the duration of the IOP, though a near-isothermal layer developed from 0800 to 1400 UTC, 19 February between the surface inversion and the capping inversion. The shallow surface inversion developed around 0200 UTC on 19 February and deepened to approx. 800 hPa by 1400 UTC. Saturation was limited to the inverted layer; there was a rapid increase in relative humidity near the surface, while relative humidity in the boundary layer remained drier.

Overall, all four cases are characterized by a nocturnal surface-based inversion and the presence of a subsidence inversion, creating a calm, stable environment with saturation at the surface that might support fog. However, fog only formed in some instances. Although a stable mixed-layer and surface-based inversion with saturation at the surface form during all IOPs, the distribution of relative humidity in the boundary layer marks a distinction between fog and clear cases: a layer with saturation conditions developed in the stable boundary layer during the clear IOPs, while during foggy IOPs, saturation was concentrated near the surface with drier air in the stable boundary layer. A notable moisture gradient exists between the near-surface layer and the stable boundary layer during fog IOPs. In addition, the depth and strength of the inversion differ between fog cases (e.g., IOPs 6 and 8) and may be independent of fog formation. This motivates us to further examine surface and near-surface conditions.

4.2 | Surface and near-surface conditions

While all cases took place under a synoptic ridge, the timing of the ridge impacted fog formation. As can be seen in Figure 4a, the surface pressure during these selected IOPs demonstrates two distinct classes: during fog events (IOPs 6 and 8), there was relatively steady pressure as a high-pressure center was already established over Heber, while during non-fog events (IOPs 3 and 7), the pressure steadily increased as a high-pressure center approached Heber.

Net longwave radiation at the surface can deduce the impact of cloud cover on radiation-type fog (Figure 4b). Generally, IOPs 6 and 8 were clear, confirming the radiative cooling as shown in Figure 3. Occasional clouds during IOP 7 limited radiative cooling. Overcast conditions prevailed during most of IOP 3. We can classify fog cases as those that remained clear due to a dominant high-pressure center, while disturbed, cloudy conditions are not associated with fog.

Calm near-surface wind plays a vital role in fog formation. The wind's behavior during the daytime was distinct between fog and non-fog cases (Figure 4c): During the non-fog IOPs (3 and 7), daytime winds were more vigorous, consistent with some disturbance, such as an approaching high-pressure system, while during the fog IOPs (6 and 8), daytime winds were not as strong (maximum wind of ~2 $m \cdot s^{-1}$), consistent with an established high-pressure center over Heber and overall calm conditions. The nocturnal winds during all IOPs were mostly quiet, typically less than 2 $m \cdot s^{-1}$. The wind direction was highly variable and less consistent (no shown) under those calm conditions (wind speed was less than 1–2 $m \cdot s^{-1}$). Therefore, while calm wind is necessary for fog formation, there was no wind direction associated with fog.

The nighttime temperature during all cases was similar, decreasing to roughly −10°C each night (Figure 4d). However, during the foggy IOPs 6 and 8, the diurnal temperature range was much more significant than observed in the clear cases. The temperature range was roughly 18°C during IOP 6 and approx. 16°C during IOP 8. In comparison, during IOP 3, the range was approx. 14°C, and approx.12°C during IOP 7 (Figure 4d). This should be a critical difference between foggy and clear events, as the warmer daytime temperatures may have led to the melting of snow or ice and provided more available surface

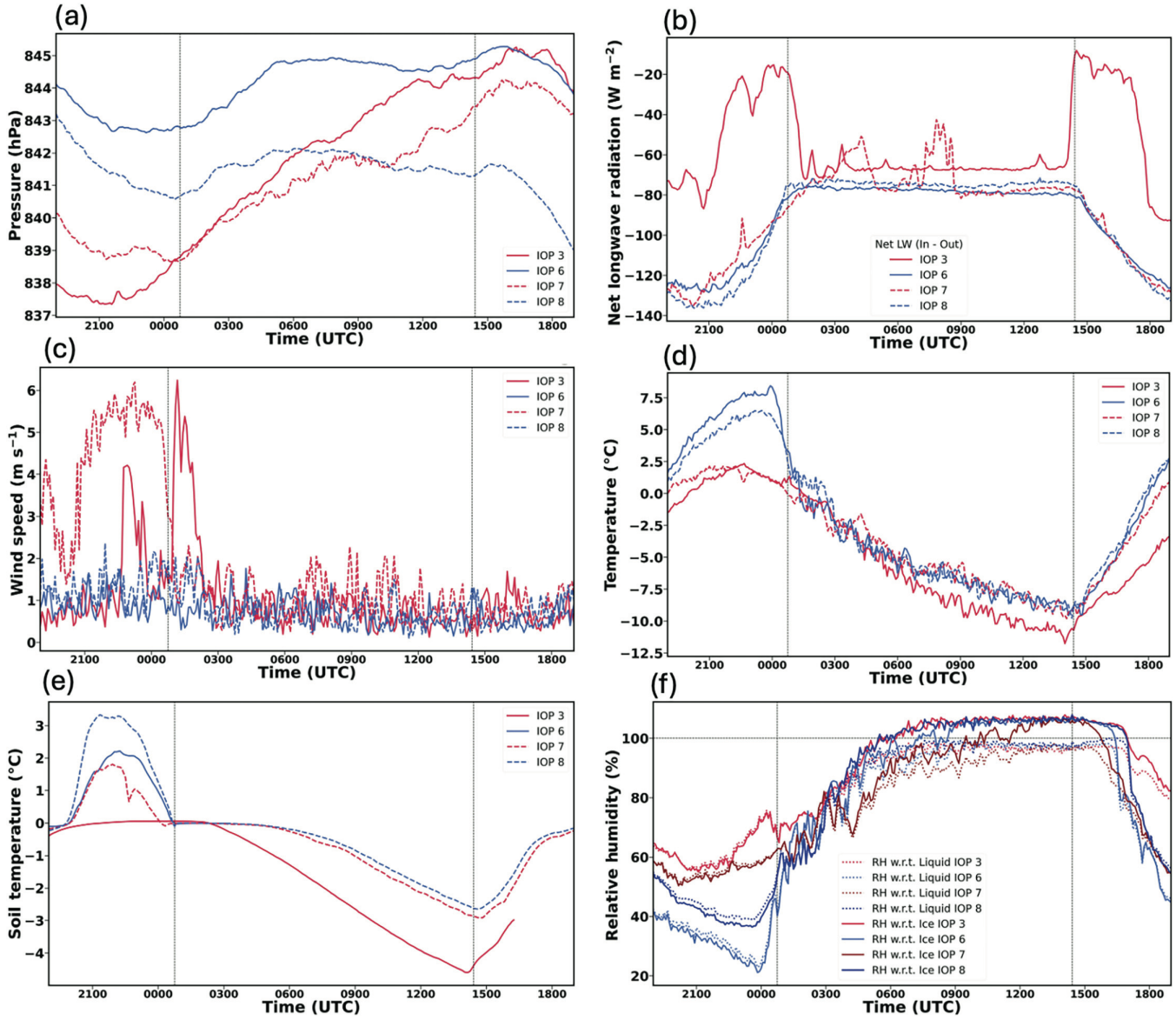

FIGURE 4 Comparison of meteorological conditions during intensive observing periods (IOPs) 3, 6, 7, and 8 at the Deer Creek Supersite of (a) 2-m surface pressure (hPa), (b) 2-m net longwave radiation ($W \cdot m^{-2}$), (c) 2-m wind speed ($m \cdot s^{-1}$), (d) 2-m temperature (°C), (e) soil temperature at 0.6 cm (°C), (f) 2-m relative humidity (%) with respect to ice (solid) and liquid (dotted).

moisture. During the nighttime, the sharper decrease in temperature should enhance condensation and sublimation, leading to fog formation.

The soil conditions in Heber Valley (Figure 4e) varied throughout the campaign, with periods of melting, freezing, and precipitation leading to frequent phase changes of soil water. These conditions complicate applying soil moisture variables; therefore, soil temperature at a depth of 0.6 cm was used to examine the processes taking place during the fog and non-fog IOPs. Due to the patchy, thin snow that characterized most of the campaign, the soil was not well insulated. The intense daytime heating during the fog IOPs penetrated the soil, and there was a strong coupling between the air and soil temperatures. The foggy IOPs had soil temperatures well above freezing, with the warmest cases resulting in fog (Figure 4e).

Finally, the importance of relative humidity is evidenced, as saturation is necessary for fog formation. Nevertheless, it is not a metric for differentiating the likelihood of fog formation, as near-surface conditions achieved saturation independent of whether fog formed or not (Figure 4f). Throughout the campaign, we consistently observed saturated near-surface conditions resulting in frost and riming on the surface, even as the available moisture sources froze over and the snow melted.

4.3 | Turbulence

While there has been debate about the role of turbulence in fog formation in previous studies (Li & Pu, 2022; Musson-Genon, 1987; Roach et al., 1976), CFACT observations offer an excellent opportunity to characterize the presence of turbulence during fog formation and evolution. Using the 32-m tower data, turbulence kinetic energy (TKE) is calculated according to Stull (1988); winds are represented as the sum of the mean (average) flow and turbulence:

$$u = \overline{u} + u'. \tag{1}$$

The average flow can be calculated in several ways, either as block or running averages. A 5-min centered block average of the 20-Hz winds was used. TKE measures the kinetic energy of the turbulent portion of the flow. Instantaneous TKE (ITKE) can be calculated as

$$\mathrm{ITKE} = \frac{1}{2}\left(u'^2 + v'^2 + w'^2\right). \tag{2}$$

However, instantaneous TKE can vary considerably, so it is useful to take a time-averaged mean TKE that is more representative:

$$\mathrm{TKE} = \frac{1}{2}\left(\overline{(u-\overline{u})^2} + \overline{(v-\overline{v})^2} + \overline{(w-\overline{w})^2}\right). \tag{3}$$

For this analysis, a 5-min centered block average of the TKE was selected, as a longer averaging period represented a change in the TKE signal. Tests with various averages indicated that 5 min was an inflection point.

Figure 5 presents 5-min averages of TKE during the four IOPs. Ultimately, we found overall low TKE conditions ranging from 0 to 0.75 $m^2 \cdot s^{-2}$ throughout the lower boundary layer during fog formation and some periods of increased TKE before fog formation. Notably, there was a period of higher TKE during IOP 8, which may have supported a more extended period of fog than during IOP 6, which had weaker turbulence. Meanwhile, fog was observed in the period (marked by red lines in Figure 5b,d) of the weakest TKE. The TKE values in Figure 5b also indicate a threshold value of roughly 0.5 $m^2 \cdot s^{-2}$, where a period of elevated TKE assisted in mixing the near-surface layer. During the nocturnal period, the null cases (Figure 5a for IOP 3 and Figure 5c for IOP 7) were nearly as calm as the fog cases within the lower boundary layer.

IOP 6 (Figure 5b) was fairly turbulent, with higher turbulence near the surface and extending upward. There was significant TKE in the afternoon which was maximized around 2100 UTC 12 February and decreased considerably in frequency, extent, and magnitude after sunset. Nocturnal turbulence was present, though it was temporally and spatially distributed throughout the lower boundary layer. During the other fog case, IOP 8 (Figure 5d), the fog was observed when TKE decreased to roughly 0.5 $m^2 \cdot s^{-2}$ after being preceded by increased TKE in the evening. However, while the duration of the elevated TKE period was similar to that of IOP 6, the overall TKE throughout the afternoon was lower. Notably, the early evening was characterized by a strong, short-lived spike in TKE throughout the lower boundary layer, as opposed to the weaker pockets of TKE that took place throughout the early evening in IOP 6. This stronger period of TKE extended throughout the lower boundary layer (up to 32 m) and may have helped to mix the layer thoroughly (in particular, to vertically mix surface and soil moisture in the boundary layer) and supported more persistent fog.

The behavior of TKE during IOP 8 (Figure 6d) was almost identical to that during IOP 6 (Figure 6b), except that TKE during IOP 8 was nearly twice as strong. In these cases (IOPs 6 and 8), turbulence may have been beneficial, even necessary, for fog to form. However, similar conditions during IOPs 3 and 7 did not result in fog. In the null cases, IOP 3 (Figure 6a) and 7 (Figure 6c), both had increased turbulence during the afternoon and evening, which calmed to below the threshold (0.5 $m^2 \cdot s^{-2}$), in accordance with the behavior during the fog cases. It is difficult to determine the influence of turbulence on these cases, as several other factors have been identified that made these cases less than ideal, including cloud cover, wind, and cool daytime temperatures.

4.4 | Conditions supporting fog formation

The findings from the previous sections are summarized in Table 1. From this summary, variables can be identified that clearly differentiate between clear and foggy events. Synoptic conditions strongly affect local near-surface and boundary-layer conditions, which in turn are the determining factors in fog formation. We found that an established high-pressure ridge over the Great Basin with associated local clear skies was ideal for fog formation. Other local surface and boundary-layer conditions that were ideal for fog formation include the following: a near-surface inversion with saturation near the surface and a strong moisture gradient in the boundary layer; calm winds for the duration of IOP; warm (above-freezing) daytime air temperatures with a large diurnal range, accompanied by warm daytime soil temperatures; a period of increased turbulence kinetic energy (above 0.5 $m^2 \cdot s^{-2}$), followed by calm conditions throughout the fog duration; and supersaturation with respect to ice.

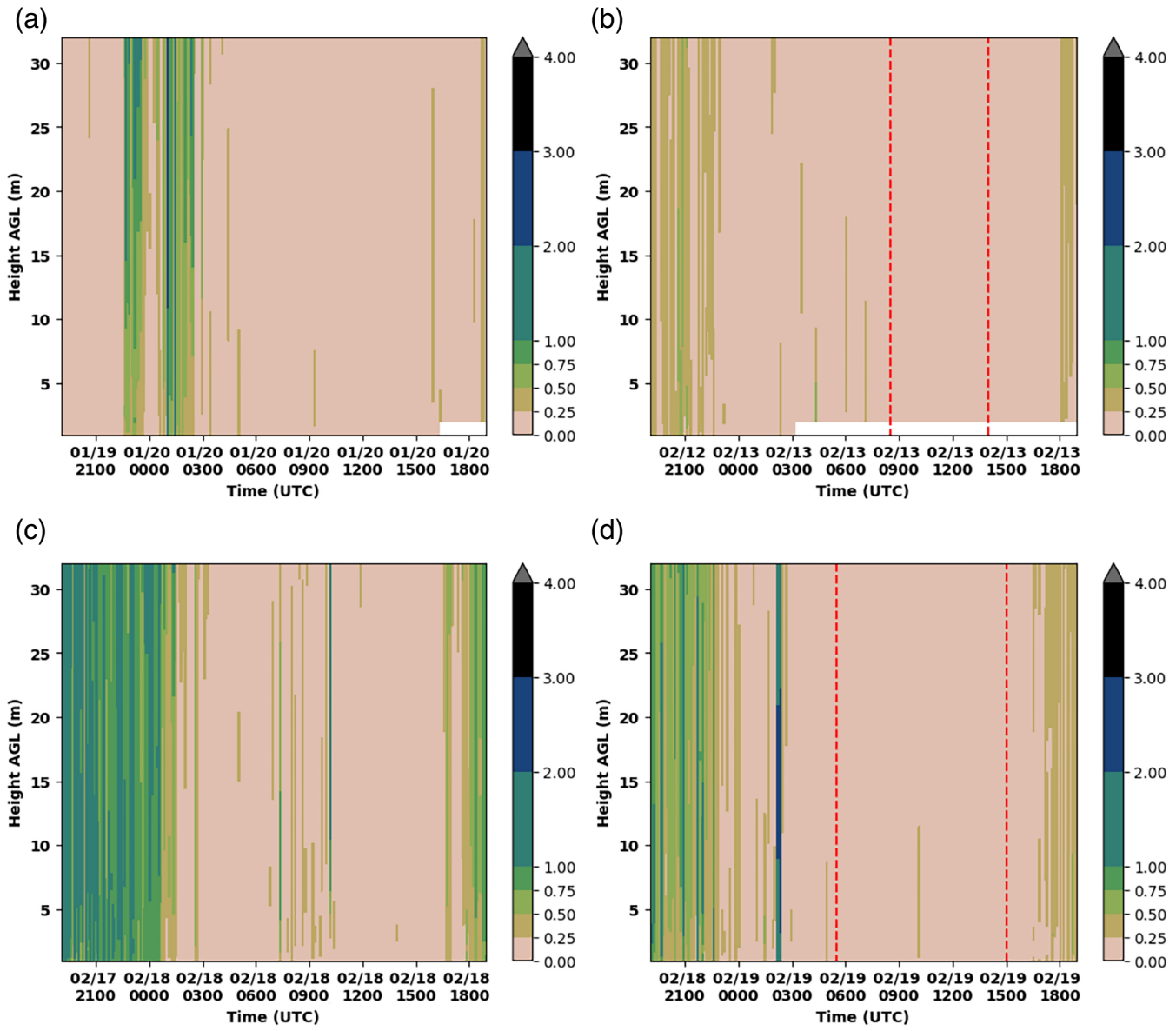

FIGURE 5 Contours of 5-min averaged turbulence kinetic energy (TKE, $m^2 \cdot s^{-2}$) from 1 to 32 m at the Deer Creek Supersite during (a) Intensive Observing Period (IOP) 3, (b) IOP 6, (c) IOP 7, and (d) IOP 8. The interval between the two red lines highlights the period when fog was observed. AGL, above ground level.

We hypothesize that this set of identified factors could potentially be applied to fog prediction in weather forecasting. Therefore, we first apply them in the WRF model validation to confirm this possibility.

5 | EVALUATION OF WRF SIMULATION

As mentioned above, IOPs 3, 7, and 8 were predicted as fog cases (in reality, only IOP 8 was a fog case) during the field campaign, while IOP 6 was forecasted as a clear, quiescent case (but fog did occur) by the conditions produced with the WRF model. With the key factors supporting fog formation identified in the previous sections, we evaluate why the WRF outputs are helpful or not helpful in producing accurate fog forecasts.

CFACT IOPs occurred from 1900 to 1900 UTC (noon to noon local time). The model forecast initialized at 0000 UTC on the first day of the IOP was used as an essential reference to finalize the deployment decision. Therefore, the WRF output and observations were compared for this set of forecasts for each case. For example, during IOP 6, which took place from 1900 UTC, 12 February to 1900 UTC, 13 February, model outputs initialized at 0000 UTC on 12 February were used for comparison (at 5-min

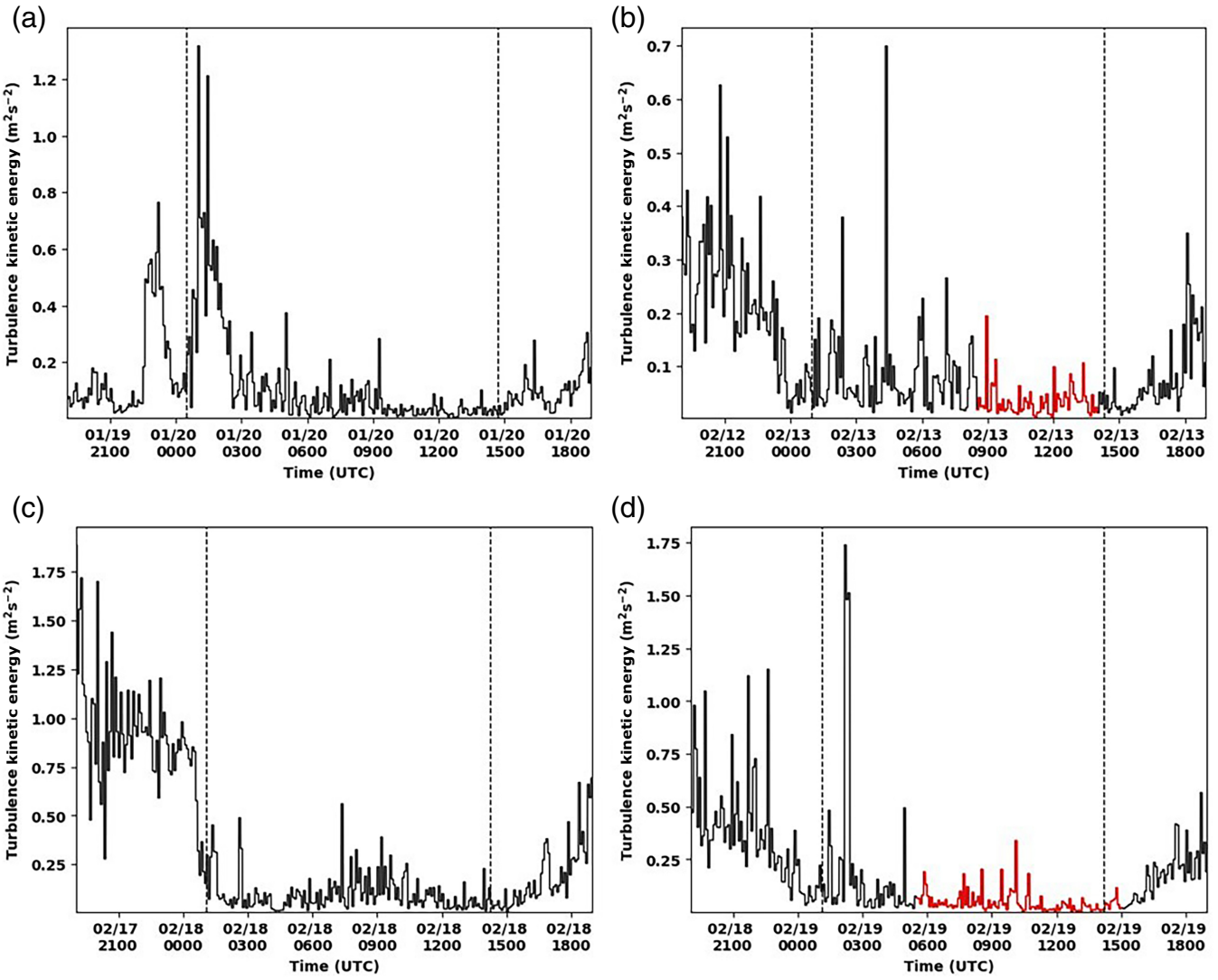

FIGURE 6 Five-min averaged turbulence kinetic energy (TKE) time series at 2 m at the Deer Creek Supersite during (a) Intensive Observing Period (IOP) 3, (b) IOP 6, (c) IOP 7, and (d) IOP 8. The red color highlights the period when fog was observed, while the black dashed lines indicate sunrise and sunset.

intervals). The evaluation emphasizes the boundary-layer and surface conditions since the WRF model captured the established ridge condition well at the synoptic scale for all cases. We first compared the model outputs with radiosonde observations to evaluate the model-simulated atmospheric profiles (Figure 7). The WRF-simulated surface variables were compared with the observations collected at the DC SS, where all fog events were observed. Only the comparison from IOP 3 (Figure 8) and IOP 8 (Figure 9) are shown, considering the similarity of figures and space limitation for the whole paper.

During IOP 3, the model simulated the overall atmospheric profile (e.g., Figure 7a–c), including wind profile (not shown) reasonably, although the strength of the capping inversion below 700 hPa was either not captured or underestimated. Surface pressure (Figure 8a) was simulated well. The incoming longwave radiation (Figure 8b) during the daytime was poorly predicted, with a period of cloud cover predicted around 0000 UTC that did not occur. This period of cloud cover lowered the air temperature (Figure 8d) by roughly 2°C. As a result, there was a sharp increase in relative humidity with respect to ice (Figure 8e) before midnight local time (0600 UTC, 20 January). The effect of the simulated clouds was also visible in the mixing ratio, specifically around 0000 and 0900 UTC; however, the overall moisture conditions were overpredicted (Figure 8g). The winds were underpredicted before 0300 UTC on 20 January, but the weak winds during the rest of the period were captured (Figure 8c).

The WRF-simulated TKE was output from the 3D TKE subgrid mixing scheme (Juliano et al., 2022) and represents a spatially averaged TKE value, whereas the TKE

TABLE 1 Summary of the near-surface and boundary-layer meteorological conditions during each IOP.

Case	IOP 3 19–20 January	IOP 6 12–13 February	IOP 7 17–18 February	IOP 8 18–19 February
Fog	No	Yes	No	Yes
Pressure/Synoptic (Figure 2)	Increasing Pressure as a high developed over Utah	**Established high pressure**	Transition following a winter storm	**Established high pressure over Utah**
Snow cover	Patchy snow across the valley floor	Very little snow cover in the valley	Almost no snow cover in the valley	Almost no snow cover in the valley
Inversion characteristics	A deep, moist inversion formed due to a subsidence inversion dropping and a surface inversion deepening, eventually joining together	A very dry, shallow inversion that strengthens overnight as the surface temperature drops	A deep, somewhat moist inversion forms as a capping inversion lowers and a surface inversion evolves upward	A deep and relatively dry inversion forms due to a capping inversion weakening as a surface inversion deepens , eventually joining together
TKE characteristics	Weak ($<0.5\ m^2 \cdot s^{-2}$) TKE conditions throughout the lower boundary layer for most of the IOP. Short periods of elevated TKE observed around the evening transition	Weak ($<0.5\ m^2 \cdot s^{-2}$) TKE conditions throughout the lower boundary layer only during the period that fog was observed. Elevated TKE in discontinuous periods throughout the lower boundary layer, decreasing in frequency and magnitude after sunset	Strongly elevated TKE in the afternoon persisting until shortly after sunset. Weak ($<0.5\ m^2 \cdot s^{-2}$) conditions exist for most of the nocturnal period, interrupted only by short-lived, slightly elevated TKE corresponding to passing clouds	Weak ($<0.5\ m^2 \cdot s^{-2}$) TKE conditions for most of the nocturnal period, with a notable period of high TKE several hours prior to fog formation and separate from the moderate TKE during the afternoon and evening
Cloud cover (Figure 3b)	Intermittent cloudy conditions during the evening and afternoon, with clear skies from 0700 to 1400 UTC	**Clear skies for the duration of the IOP**	Mostly clear, passing overcast conditions around midnight	**Clear skies for the duration of the IOP**
Air temperature (Figure 3d)	Cool (2.3°C) daytime temperatures and cold overnight temperatures (−11.8°C)	**Warm (8.4°C) daytime temperatures and cold overnight temperatures (−9.6°C)**	Cool (2.2°C) daytime temperatures and cold overnight temperatures (−9.8°C)	**Warm (6.5°C) daytime temperatures and cold overnight temperatures (−9.76°C)**
Winds (Figure 3c)	Mostly calm ($<2\ m \cdot s^{-1}$) winds with elevated winds around the evening transition	**Entirely calm ($<2\ m \cdot s^{-1}$) winds for the duration of the IOP**	Mostly calm ($<2\ m \cdot s^{-1}$) winds with elevated winds around the evening transition	**Mostly calm ($<2\ m \cdot s^{-1}$) winds with elevated winds around the evening transition**
Soil temperature (Figure 3e)	Freezing daytime soil temperatures, then below-freezing temperatures at night	**Warm (2.2°C) soil temperature during the day, then below-freezing temperatures at night**	Warm (1.8°C) soil temperature during the day, then below-freezing temperatures at night	**Warm (3.3°C) soil temperature during the day, then below-freezing temperatures at night**
Relative humidity w.r.t ice	Supersaturation reached and maintained from 0500 UTC	Persistent supersaturation reached at 0900 UTC	Supersaturation is reached at 1100 UTC	Persistent supersaturation reached at 0700 UTC

Note: Bolded sections indicate emphasis on the variable's role in fog formation.

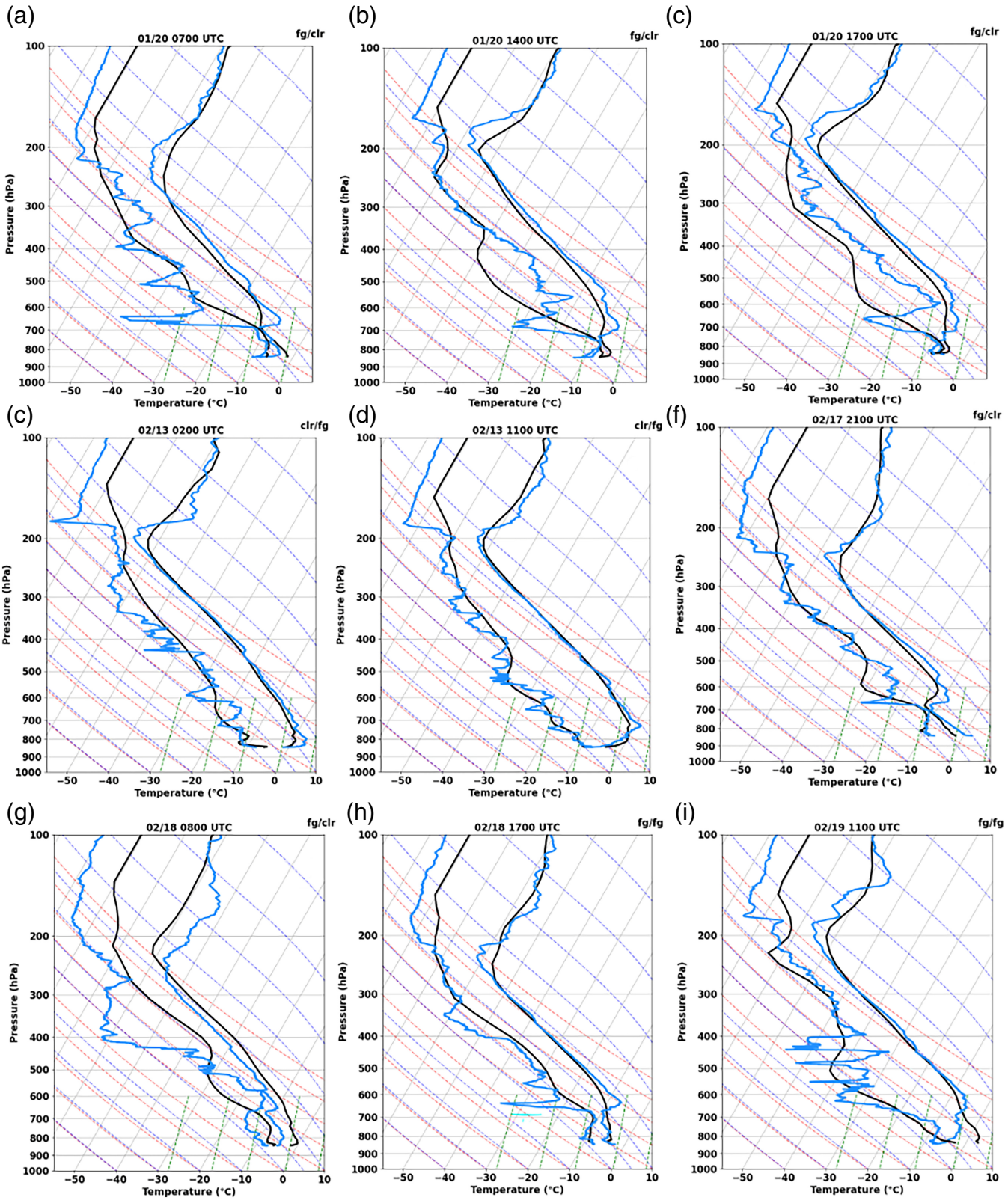

FIGURE 7 Comparison of radiosonde soundings (blue) and Weather Research and Forecasting (WRF)-simulated SKEW-Ts (black) at the Deer Creek Supersite (DC SS) during Intensive Observing Period (IOP) 3 (a–c), IOP 6 (d, e), IOP 7 (f, g), and IOP 8 (h, i) for the selected times (as shown in the title of each panel), demonstrating the evolution of the atmospheric profiles over the duration of each case. Panels were also labeled according to the fog forecast/fog occurrence, abbreviated to "fg" for fog and "clr" for clear. For instance, a "fg/clr" ("fg/fg") label indicates that fog was predicted but *did not* (*did*) occur.

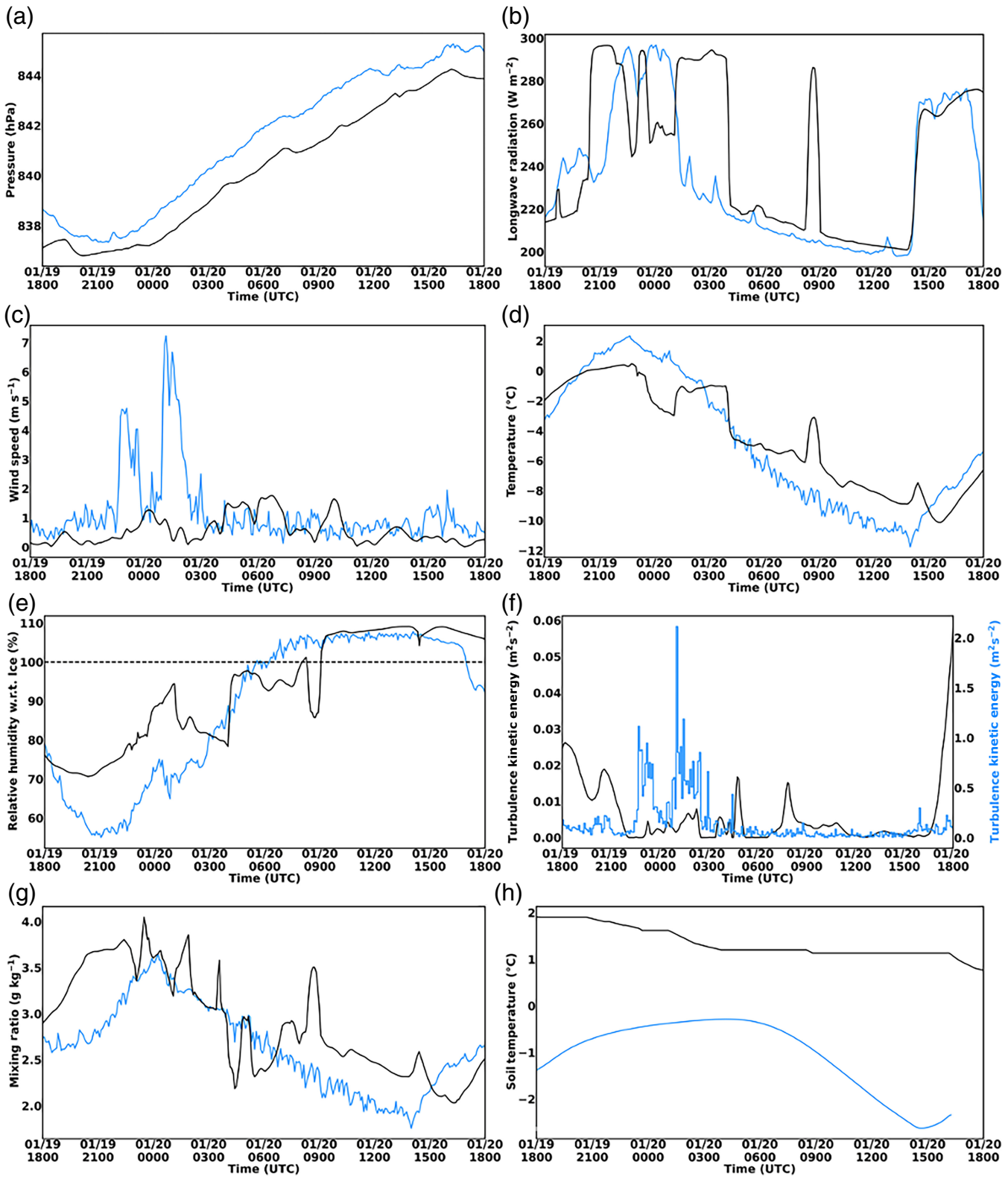

FIGURE 8 Comparison of weather research and forecasting (WRF) simulation (black) and Cold Fog Amongst Complex Terrain (CFACT) observations (blue) at the Deer Creek Supersite during Intensive Observing Period (IOP) 3. (a) 2-m pressure, (b) 2-m incoming longwave radiation, (c) 10-m simulated wind speed vs 7-m observed wind speed, (d) 2-m temperature, (e) 2-m relative humidity with respect to ice, and (f) 15-m simulated and 17-m observed turbulence kinetic energy, (g) 2-m mixing ratio, (h) 5-cm simulated soil temperature vs 4.4-cm observed soil temperature.

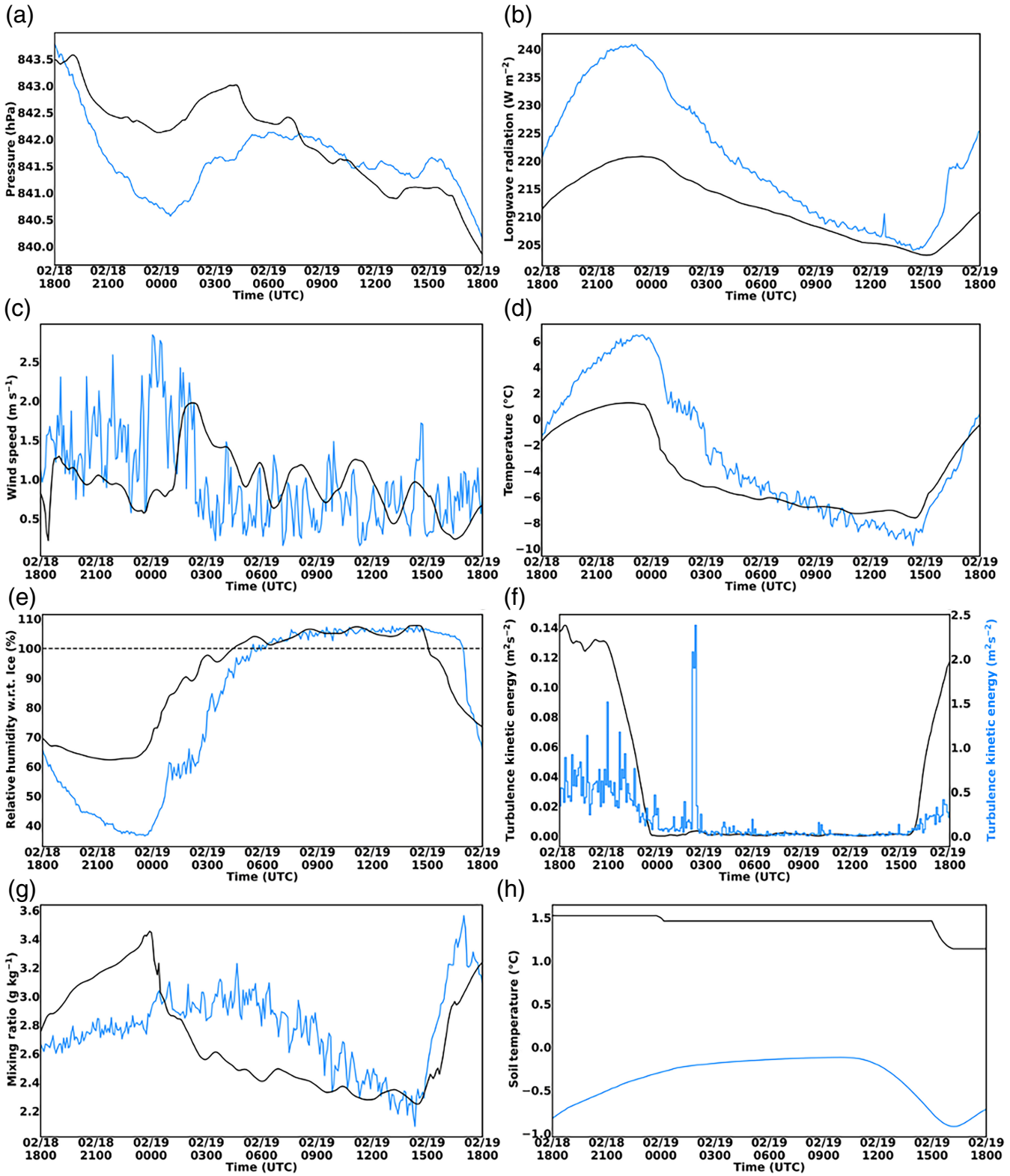

FIGURE 9 Same as Figure 8, except during IOP 8.

calculated from observations is a point value from the data collected at the DC SS. These differences in calculation lead to large discrepancies in TKE magnitude. However, the trends of TKE produced by the WRF model are comparable to those derived from the observations (Figure 8f) and thus still provide the basis for comparison for the model's prediction of TKE in the boundary layer. Notably, according to the picture taken during the field

campaign, the WRF model assumed nearly 10 cm of snow at the DC SS when there was almost no snow cover during IOP 3. The simulated soil temperature (Figure 8h) was above freezing, possibly due to the strong insulation effects of such deep snow, resulting in a major departure of diurnal variation of soil temperature from observations. Since surface conditions impact the energy budget, they influence many simulated near-surface variables. This overestimate of snow cover is present in all selected IOP cases. It is likely one of the critical variables that contribute to inaccurate fog prediction and thus will need to be improved and further studied following Zhang and Pu (2019).

For IOP 6, the model simulated the atmospheric profile (Figure 7d,e), including wind profile (not shown) very well, capturing the strength and temporal evolution of the surface inversion, although slightly underpredicting the final depth of the inversion. We also compared the surface conditions (figure not shown). The model forecasted a more consistent surface weather pattern with higher pressure. According to the longwave radiation, the model maintained clear conditions but indicated an overall colder atmosphere. Surface winds were also underpredicted, possibly due to the assumption of a more deeply developed high-pressure ridge. The timing of afternoon and overnight TKE fluctuations was well simulated, although the decrease in TKE around sunset was sudden rather than the gradual calming that was observed. Forecasted conditions represented the period of increased TKE in the daytime before calming overnight.

At the same time, WRF showed roughly 6 cm of snow, while less than 0.6 cm was measured at the DC SS. The simulated soil temperature did reach above freezing but was roughly 5°C below the observations. At night, the air temperature was overestimated and maintained milder conditions. Because the simulated temperature did not drop as low as observed, relative humidity conditions stayed dry, never reaching saturation throughout the whole IOP. Mixing ratio conditions had a strong diurnal signal, with similar underprediction overnight and overprediction during the afternoon and evening. Therefore, even with strong established high pressure over Utah, with clear skies, calm winds, and low turbulence supporting a strong, if shallow, temperature inversion, due to the surface conditions remaining unsaturated, the model did not predict the fog conditions in IOP 6.

Throughout IOP 7, the evolution of the boundary layer was predicted very well, especially concerning the location and strength of the capping inversion (Figure 7f,g). The boundary layer was simulated well; the presence of both the upper and surface inversions was captured (Figure 7f), although the duration of the surface inversion was slightly overpredicted, beginning at 0300 UTC rather than at 0500 UTC (figure not shown). Relative humidity was underpredicted above the surface due to the fact that the moist conditions were not captured after the two inversions joined. Wind conditions were simulated well, though underpredicted in the afternoon.

As for the surface conditions for the IOP 7 case (figure not shown), the surface pressure trend was well represented, with the model simulating an approaching high-pressure system in the vicinity. During the transition period from one weather pattern to another, cloud cover was present, though it was underestimated in the model. Notably, the model did not simulate a passing band of clouds around 0300 UTC and underestimated the resulting longwave radiation from another cloud band around 0700 UTC. This may correspond with the predicted overall dry atmospheric conditions. The cloud cover that was predicted limited radiative cooling and led to a slight increase in surface temperature and a decrease in relative humidity. Overall, the model underpredicted surface temperature throughout the day. The model predicted less disturbed weather conditions with clearer skies and much calmer winds, leading to greater radiative cooling than observed and resulting in a significant overprediction of relative humidity. The actual near-surface moisture was underestimated and was more sensitive to cloud cover in the simulation than was observed. TKE trends were predicted well. However, the elevated TKE in WRF outputs was a result of a simulated typical convective boundary layer, while the observed high TKE was due to strong winds from disturbed conditions. IOP 7 was a null case where fog was not observed; however, the model simulated calm, cold, and moist conditions that overpredicted suitability for fog.

During IOP 8, the model represented the boundary layer evolution, predicting the surface inversion (Figure 7h,i) with an overall underprediction of the strength and extent of the final inversion (1100 UTC) in the boundary layer. Surface conditions were predicted well overall, with accurate pressure conditions (Figure 9a) and clear skies (Figure 9b). Winds were simulated very well, capturing the magnitude of daytime wind and delayed by only roughly an hour (Figure 9c). An increase in TKE around 0200 UTC was predicted with accurate timing, although the magnitude was underpredicted (Figure 9f). The trend in air temperature was well simulated, but similar to IOPs 3 and 6, maximum daytime temperatures were underpredicted and minimum nighttime temperatures were overpredicted. The maximum simulated daytime temperatures were only slightly above freezing. At the same time, the observed temperatures were over 6°C (Figure 9d). Soil temperature (Figure 9h) was also simulated as warmer than observed, consistent with the simulations during other IOPs. Mixing ratio conditions were also mis-forecasted somewhat with overprediction of the available moisture in the daytime and then underprediction at

night (Figure 9g). Overall, the clear skies, calm winds, and radiative cooling led to the surface reaching saturation at almost the same time as in observations (Figure 9e). These conditions were beneficial for fog formation. Thus, fog during IOP 8 was forecasted well using the WRF model.

6 | SUMMARY AND DISCUSSION

The CFACT field campaign in Heber Valley, northern Utah, USA, was dedicated to studying cold fog over complex terrain using IOPs. Utilizing the CFACT field observations for two mountainous ephemeral fog cases and two null fog cases, this study found that the ideal conditions for wintertime ephemeral radiation fog include the following (as summarized in Table 1):

- an established high pressure over the Great Basin, clear skies in the local area;
- dry inverted conditions, with saturation near the surface and strong moisture gradient within the boundary layer;
- calm winds for the duration of the diurnal cycle;
- warm (above-freezing) air temperatures during the daytime create an extensive diurnal range. in addition, warm (above-freezing) soil temperatures linked with the warm air temperature during the daytime could play a role;
- a period of increased (above 0.5 $m^2 \cdot s^{-2}$) turbulence and then calm conditions for the duration of the fog;
- supersaturation with respect to ice.

Conditions that may suppress fog have also been outlined, including the following: an approaching high-pressure pattern; cloudy conditions; moist inverted conditions; increased winds during the daytime; freezing or near-freezing air temperatures during the daytime; and freezing or near-freezing soil temperatures during the daytime.

A high-resolution WRF model provided real-time forecasts for the area, with insight into possible fog occurrences during the campaign. The model outputs allowed an opportunity to compare the simulated and observed surface and boundary-layer conditions. High-resolution WRF model forecasts were evaluated with CFACT observations and guided by the findings from the observations regarding the factors supporting fog formation. Of the four cases studied, results show that the successful prediction of these identified factors from the observations is crucial for the successful prediction of fog by the numerical model. Specifically, the model predicted large-scale weather processes and overall atmospheric conditions well. However, due to failures in predicting some key surface and boundary-layer conditions, possibly due to the impacts of complex terrain, the WRF model did not correctly predict the fog occurrence or non-fog conditions for IOPs 3, 6, and 7. Meanwhile, even with forecast biases, since the WRF model reproduced these conditions supporting fog formation, the fog was correctly predicted for IOP 8.

The outcomes of this study identified key factors that support ephemeral mountainous fog formation, which can be applied in future fog weather forecasting and model evaluation. Since mountainous terrain and atmospheric conditions are characterized by their strongly heterogeneous nature, meteorological conditions vary from one station to another; fog forms locally. Results from this study also suggest the necessity of similar investigation in future studies. First, surface temperature conditions during clear and calm conditions were poorly predicted (the simulations were generally too cold during the day and too warm at night), indicating that near-surface processes related to turbulence fluxes and possibly radiation flux divergence in WRF need to be improved. These issues have been observed in WRF under summertime conditions in Utah basins as well (Massey et al., 2014; Zhang et al., 2013). Meanwhile, katabatic winds, drainage flow, and topography play roles in fog formation. Their contributions should have been included in the meteorological conditions considered in this study. However, understanding their specific roles in fog formation can still be a research topic to explore in the future. In addition, due to the unusual climate conditions during the campaign, where Utah was under a severe drought, the model predicted typical snow conditions while record-setting minimum snowfall actually took place. Previous studies have investigated the sensitivity of the WRF model to snow conditions in Heber Valley (Zhang & Pu, 2019) and found that increasing snow depth and albedo improved the prediction of fog. Although the 2022 winter was marked by a significant snow drought, limiting available moisture, snowmelt and sublimation during warm days may have been a substantial source of moisture necessary for fog formation and are positively correlated to fog occurrence. Future work will include sensitivity studies on model surface and near-surface conditions, especially snow, soil state, and surface parameterizations.

Moreover, in addition to meteorological conditions, microphysical processes play an essential role in fog formation. The visibility algorithm of the numerical model relies a great deal on microphysical processes. Future work will emphasize the study of microphysical process parameterizations and visibility algorithms in numerical models and their relationship to fog.

ACKNOWLEDGEMENTS

This study is supported by US National Science Foundation (NSF) Award #2049100. The computational resources and support from the UCAR CISL supercomputing system and the Center for High-Performance Computing (CHPC) at the University of Utah are appreciated. The NCEP NAM data are obtained from the NCAR Research Data Archive (https://rda.ucar.edu/datasets/ds609.0/). The CFACT field campaign catalog and observations are available at a data repository managed by NCAR's Earth Observing Laboratory at https://catalog.eol.ucar.edu/cfact.

FUNDING INFORMATION

This study is supported by NSF Award #2049100.

DATA AVAILABILITY STATEMENT

The NCEP NAM data are obtained from the NCAR Research Data Archive (https://rda.ucar.edu/datasets/ds609.0/). The CFACT field campaign catalog and observations are available at a data repository managed by NCAR's Earth Observing Laboratory at https://catalog.eol.ucar.edu/cfact.

ORCID

Zhaoxia Pu https://orcid.org/0000-0003-4461-1789

REFERENCES

Adedokun, J.A. & Holmgren, B. (1993) Acoustic sounder doppler measurement of the wind fields associated with a mountain stratus transformed into a valley fog: a case study. *Atmospheric Environment Part A General Topics*, 27, 1091–1098.

American Meteorological Society. (2012) Fog Glossary of meteorology.

Ashley, W.S., Strader, S., Dziubla, D.C. & Haberlie, A. (2015) Driving blind: weather related vision hazards and fatal motor vehicle crashes. *Bulletin of the American Meteorological Society*, 96, 755–778.

Clayton, J., Brosten, T., Sutcliffe, K., Eiriksson, D., Burly, J., Byington, J. et al. (2022a) Utah water supply outlook report. NRCS WSOR, pp. 66.

Clayton, J., Brosten, T., Sutcliffe, K., Eiriksson, D., Burly, J. & Neff, D. (2022b) Utah water supply outlook report. NRCS WSOR, pp. 65.

Cuxart, J. & Jiménez, M.A. (2012) Deep radiation fog in a wide closed valley: study by numerical modeling and remote sensing. *Pure and Applied Geophysics*, 169, 911–926.

Ducongé, L., Lac, C., Vié, B., Bergot, T. & Price, J.D. (2020) Fog in heterogeneous environments: the relative importance of local and non-local processes on radiative-advective fog formation. *Quarterly Journal of the Royal Meteorological Society*, 146, 2522–2546.

Federal Aviation Administration. (2010) Weather-related aviation accident study: 2003–2007.

Fernando, H.J.S. & Coauthors (2021) C-FOG: Life of Coastal Fog. *Bulletin of the American Meteorological Society*, 102, E244-E272. https://doi.org/10.1175/BAMS-D-19-0070.1

Fernando, H.J.S., Pardyjak, E.R., Di Sabatino, S., Chow, F.K., De Wekker, S.F., Hoch, S.W. et al. (2015) The MATERHORN – unraveling the intricacies of mountain weather. *Bulletin of the American Meteorological Society*, 96, 1945–1967.

Fitzjarrald, D.R. & Lala, G.G. (1989) Hudson valley fog environments. *Journal of Applied Meteorology and Climatology*, 28, 1303–1328.

Fultz, A.J. & Ashley, W.S. (2016) Fatal weather-related general aviation accidents in the United States. *Physical Geography*, 37, 291–312.

Fuzzi, S., Facchini, M.C., Orsi, G., Lind, J.A., Wobrock, W., Kessel, M. et al. (1992) The po valley fog experiment 1989. *Tellus B*, 44, 448–468.

Ghude, S.D., Bhat, G.S., Prabhakaran, T., Jenamani, R.K., Chate, D.M., Safai, P.D. et al. (2017) Winter fog experiment over the Indo-Gangetic plains of India. *Current Science*, 112, 767–784 http://www.jstor.org/stable/24912578

Golding, B.W. (1993) A study of the influence of terrain on fog development. *Monthly Weather Review*, 121, 2529–2541.

Gultepe, I. & Coauthors (2021) A review of coastal fog microphysics during C-FOG. *Boundary-Layer Meteorology*, 181, 227-265. https://doi.org/10.1007/s10546-021-00659-5

Gultepe, I., Fernando, H.J.S., Pardyjak, E.R., Hoch, S.W., Silver, Z., Creegan, E. et al. (2016) An overview of the MATERHORN fog project: observations and predictability. *Pure and Applied Geophysics*, 173, 2983–3010.

Gultepe, I., Heymsfield, A., Gallagher, M., Ickes, L. & Baumgardner, D. (2017) Ice fog: the current state of knowledge and future challenges. *Meteorological Monographs*, 58, 4.1–4.24.

Gultepe, I., Huhn, T., Pavolonis, M., Calvert, C., Gurkha, J., Heymsfield, A.J. et al. (2014) Ice fog in arctic during FRAM-ice fog project: aviation and nowcasting applications. *Bulletin of the American Meteorological Society*, 95, 211–226.

Gultepe, I., Pearson, G., Milbrandt, J.A., Hansen, B., Platnick, S., Taylor, P. et al. (2009) The fog remote sensing and modeling field project. *Bulletin of the American Meteorological Society*, 90, 341–360.

Gultepe, I., Tardif, R., Michaelides, S.C., Cermak, J., Bott, A., Bendix, J. et al. (2007) Fog research: a review of past achievements and future perspectives. *Pure and Applied Geophysics*, 164, 1121–1159.

Hang, C., Nadeau, D.F., Gultepe, I., Hoch, S.W., Román-Cascón, C., Pryor, K. et al. (2016) A case study of the mechanisms modulating the evolution of valley fog. *Pure and Applied Geophysics*, 173, 3011–3030.

Hodges, D. & Pu, Z. (2015) The climatology, frequency, and distribution of cold season fog events in northern Utah. *Pure and Applied Geophysics*, 173, 3197–3211.

Holets, S. & Swanson, R.N. (1981) High-inversion fog episodes in central California. *Journal of Applied Meteorology and Climatology*, 20, 890–899.

Juliano, T.W., Kosović, B., Jiménez, P.A., Eghdami, M., Haupt, S.E. & Martilli, A. (2022) "Gray zone" simulations using a three-dimensional planetary boundary layer parameterization in the weather research and forecasting model. *Monthly Weather Review*, 150, 1585–1619.

Li, X. & Pu, Z. (2022) Turbulence effects on the formation of cold fog over complex terrain with large-eddy simulation. *Geophysical Research Letters*, 49, e2022GL098792. Available from: https://doi.org/10.1029/2022GL098792

Massey, J.D., Steenburgh, W.J., Hoch, S.W. & Knievel, J.C. (2014) Sensitivity of near-surface temperature forecasts to soil properties over a sparsely vegetated dryland region. *Journal of Applied Meteorology and Climatology*, 53, 1976–1995.

Musson-Genon, L. (1987) Numerical simulation of a fog event with a one-dimensional boundary layer model. *Monthly Weather Review*, 115, 562–607.

National Drought Mitigation Center, U.S. Department of Agriculture, National Oceanic and Atmospheric Administration, University of Nebraska-Lincoln. (2022) United States drought monitor. https://droughtmonitor.unl.edu/data/png/20220208/20220208&uscore;west&uscore;text.png

NationalWeather Service. (2022) Weather Related Fatality and Injury Statistics. https://www.weather.gov/hazstat/

Noonkester, V.R. (1979) Coastal marine fog in southern California. *Monthly Weather Review*, 107, 830–851.

Price, J.D., Lane, S., Boutle, I.A., Smith, D.K.E., Bergot, T., Lac, C. et al. (2018) LANFEX: a field and modeling study to improve our understanding and forecasting of radiation fog. *Bulletin of the American Meteorological Society*, 99, 2061–2077.

Prtenjak, T.M., Klaić, M., Jeričević, A. & Cuxart, J. (2018) The interaction of the downslope winds and fog formation over the Zagreb area. *Atmospheric Research*, 214, 213–227.

Pu, Z., Cachere, C.N., Hoch, S.W., Pardyjak, E. & Gultepe, I. (2016) Numerical prediction of cold season fog events over complex terrain: the performance of the WRF model during MATERHORN-fog and early evaluation. *Pure and Applied Geophysics*, 173, 3165–3186.

Pu, Z., Pardyjak, E.R., Hoch, S.W., Gultepe, I., Hallar, A.G., Perelet, A. et al. (2023) Cold fog amongst complex terrain. *Bulletin of the American Meteorological Society*, 104, 2030–2052.

Roach, W.T., Brown, R., Caughey, S.J., Garland, J.A. & Readings, C.J. (1976) The physics of radiation fog: I - a field study. *Quarterly Journal of the Royal Meteorological Society*, 102, 313–333.

Skamarock, W.C., Klemp, J.B., Dudhia, J., Gill, D.O., Liu, Z., Berner, J. et al. (2021) A description of the advanced research WRF model version 4.3. NCAR Tech. Note, 556, pp. 165. https://doi.org/doi:10.5065/1dfh-6p97

Smith, D., Renfrew, I.A., Dorling, S.R., Price, J. & Boutle, I.A. (2020) Sub-km scale numerical weather prediction model simulations of radiation fog. *Quarterly Journal of the Royal Meteorological Society*, 147, 746–763.

Steeneveld, G.J., Ronda, R.J. & Hotslag, A.A.M. (2015) The challenge of forecasting the onset and development of radiation fog using mesoscale atmospheric models. *Boundary-Layer Meteorology*, 154, 265–289.

Stull, R.B. (1988) Application of the governing equations to turbulent flow. In: Stull, R.B. (Ed.) *An introduction to boundary layer meteorology*. Dordrecht: Springer, pp. 75–114.

U.S. Federal Highway Administration. (2020) How do weather events impact roads? https://ops.fhwa.dot.gov/weather/q1&uscore;roadimpact.htm

Underwood, S.J., Ellrod, G.P. & Kunhert, A.L. (2004) A multiple-case analysis of nocturnal radiation-fog development in the central valley of California utilizing the GOES nighttime fog product. *Journal of Applied Meteorology and Climatology*, 43, 297–311.

Wei, L., Pu, Z. & Wang, S. (2013) Numerical simulation of the life cycle of a persistent wintertime inversion over Salt Lake City. *Boundary Layer Meteorology*, 148(2), 399–418. Available from: https://doi.org/10.1007/s10546-013-9821-2

Zhang, F. & Pu, Z. (2019) Sensitivity of numerical simulations of near-surface atmospheric conditions to snow depth and surface albedo during an ice fog event over Heber Valley. *Journal of Applied Meteorology and Climatology*, 58, 797–811.

Zhang, H., Pu, Z. & Zhang, X. (2013) Examination of errors in near-surface temperature and wind from WRF numerical simulations in regions of complex terrain. *Weather and Forecasting*, 28, 893–914.

How to cite this article: Beal, R.L., Pu, Z., Pardyjak, E., Hoch, S. & Gultepe, I. (2024) Evaluation of near-surface and boundary-layer meteorological conditions that support cold-fog formation using Cold Fog Amongst Complex Terrain field campaign observations. *Quarterly Journal of the Royal Meteorological Society*, 150(764), 4329–4347. Available from: https://doi.org/10.1002/qj.4818